

Topography-Generated Submesoscale Coherent Vortices in the Kuroshio–Oyashio Extension Region from High-Resolution Simulations

RUICHEN ZHU,^a HAIYUAN YANG,^a ZHAOHUI CHEN,^a ZHIYOU JING,^b ZHIWEI ZHANG,^a BINGRONG SUN,^a
AND LIXIN WU^{a,c}

^a Frontier Science Center for Deep Ocean Multispheres and Earth System (FDOMES) and Physical Oceanography Laboratory, Ocean University of China, Qingdao, China

^b State Key Laboratory of Tropical Oceanography, South China Sea Institute of Oceanology, Chinese Academy of Sciences, Guangzhou, China

^c Laoshan Laboratory, Qingdao, China

(Manuscript received 27 April 2023, in final form 8 September 2023, accepted 23 October 2023)

ABSTRACT: A variety of submesoscale coherent vortices (SCVs) in the Kuroshio Extension region have been reported by recent observational studies, and the preliminary understanding of their properties, spatial distribution, and possible origins has progressively improved. However, due to relatively sparse in situ observations, the generation mechanisms of these SCVs and associated dynamic processes remain unclear. In this study, we use high-resolution model simulations to fill the gaps of the in situ observations in terms of the three-dimensional structures and life cycles of SCVs. Vortex detection and tracking algorithms are adopted and the characteristics of warm-core and cold-core SCVs are revealed. These vortices have finite Rossby numbers (0.25–0.4), and their horizontal structures can be well described by the Taylor vortex model in terms of the gradient wind balance. The vertical velocity field is characterized by a distinct dipole pattern with upwelling and downwelling cells at the vortex edge. It is very likely that both types of SCVs are generated along the eastern Japan coast through flow–topography interactions, and the Izu–Ogasawara Ridge and Hokkaido slope are found to be two important generation sites where topography friction produces extremely low potential vorticity. After leaving the boundary, SCVs can propagate over long distances and trap a water volume of $\sim 10^{11}$ m³.

KEYWORDS: North Pacific Ocean; Boundary currents; Eddies; Topographic effects

1. Introduction

Submesoscale coherent vortices (SCVs; McWilliams 1985) are a class of relatively small, subsurface intensified eddies with distinct dimensions and dynamics compared to larger mesoscale eddies. In general, they are characterized by a horizontal scale smaller than the Rossby deformation radius and an interior velocity core within or below the pycnocline. The majority of SCVs are anticyclonic with a convex lens shape with respect to the density field (McWilliams 2016). The rapid rotation at the edge of SCVs forms a dynamic barrier that limits the lateral exchange between the vortex core and the surrounding waters, which allows SCVs to survive for several years and transport physical/biogeochemical tracers thousands of kilometers away from their generation sites (e.g., Armi et al. 1989; Bower et al. 2013; Bosse et al. 2019). At the

vortex edge, the associated ageostrophic secondary circulation provides efficient routes for nutrient fluxes from the ocean interior into the euphotic zone, leading to enhanced primary production and regulating the local ecosystem (Barceló-Llull et al. 2017; Bosse et al. 2017; Karstensen et al. 2017).

SCVs have been discovered in every ocean basin (McWilliams 1985; McCoy et al. 2020). In the North Atlantic Ocean, the famous type is the Mediterranean water eddy (Meddy; McDowell and Rossby 1978), which originates from the Mediterranean outflow and plays an important role in the formation of the Mediterranean salt tongue. While typically categorized as SCVs due to their initial formation process, some Meddies exhibit larger horizontal scales on the order of 10–50 km, displaying characteristics of mesoscale eddies (Bashmachnikov et al. 2015). In the Indian Ocean, the Peddies (Senjyu et al. 1998) are formed from the Persian Gulf outflow. In the eastern Pacific Ocean, the eastern boundary upwelling system is populated by the California Undercurrent eddies (Cuddies; Garfield et al. 1999) west of the U.S. coast and Poleward Undercurrent eddies (Puddies; Frenger et al. 2018) off the coast of Peru and Chile, which transport oxygen-poor and nutrient-rich water westward into the gyre interior. Along the western boundary, Kuroshio Extension intermediate-layer eddies (Kiddies; Li et al. 2017) can trap Transition Region Model Water or North Pacific Intermediate Water (Talley 1993, 1997). In high-latitude regions, several other types of SCVs exist in the Arctic Ocean and Southern Ocean (e.g., Timmermans et al. 2008; Sheen et al. 2015; Zhao and Timmermans 2015).

Although SCVs have been proven to exist, direct observations of them are still very limited because they generate few

Denotes content that is immediately available upon publication as open access.

Supplemental information related to this paper is available at the Journals Online website: <https://doi.org/10.1175/JPO-D-23-0072.s1>.

Ruichen Zhu and Haiyuan Yang contributed equally to this work.

Corresponding author: Zhaohui Chen, chenzhaohui@ouc.edu.cn

DOI: 10.1175/JPO-D-23-0072.1

© 2024 American Meteorological Society. This published article is licensed under the terms of the default AMS reuse license. For information regarding reuse of this content and general copyright information, consult the AMS Copyright Policy (www.ametsoc.org/PUBSReuseLicenses).

signals at the sea surface. As a result, they are usually observed by chance with shipboard surveys, fixed-point moorings, and autonomous sampling platforms (e.g., Lilly and Rhines 2002; Thomsen et al. 2016; Meunier et al. 2018; Steinberg et al. 2019). These observations provide information on vortex structures, core water properties and even propagation pathways that can be used to trace the possible source of SCVs. However, it is still difficult to explore the dynamic processes and mechanisms of vortex generation due to the sparsity of submesoscale-resolving observations. In this respect, high-resolution model simulations are widely used to explore SCVs. Molemaker et al. (2015) examined the California Current system using a realistic simulation with a resolution of up to 166 m. Based on their results, Cuddies are generated from the interaction between the poleward California Undercurrent and the continental slope through instability and mixing mechanisms. In the Gulf Stream region, it has been demonstrated that SCVs are generated in the wake of a deep topographic feature called the Charleston Bump due to frictional effects (Gula et al. 2019). Recently, vortex generation processes have been analyzed based on a set of idealized flow configurations, which suggests the role of flow–topography interactions in the generation of SCVs (Srinivasan et al. 2019, 2021; Jagannathan et al. 2021). In addition to flow–topography interactions, evidence for other mechanisms, such as winter convection in the northwestern Mediterranean Sea and wind-driven destruction of potential vorticity at ocean fronts, can also be found in high-resolution models (Thomas 2008; Damien et al. 2017).

The Kuroshio–Oyashio Extension (KOE) is the region in which the exchange of heat and freshwater occurs between the subtropical and subpolar gyres in the northwest Pacific Ocean. The warm and salty Kuroshio flows over the Izu–Ogasawara Ridge and departs from the coast of Japan near 35°N to become a free inertial jet. The counterpart western boundary current, the Oyashio, flows south along the eastern coast of Japan and joins this region after separating from the coast near 40°N. The KOE region is characterized by large-amplitude meanders and energetic pinch-off eddies (Qiu et al. 1991; Sasaki and Minobe 2015; Yang et al. 2018). Compared to the strong surface eddies, the SCVs in this region have received less attention. The first report was on an anticyclonic lens detected by moored current meters at 1200 m, which observed an anomalous cold water mass that probably originated north of the subarctic front (Maximenko and Yamagata 1995). Since the first deployment of Argo floats in 1999, observed temperature and salinity profiles have accumulated in the KOE region, offering a unique opportunity to study SCVs in this region (Zhang et al. 2017; Li et al. 2017; McCoy et al. 2020). In addition to the Kiddies that contain cold, fresh, oxygen-rich waters, a warm-core SCV with warm, salty, oxygen-poor anomalies was first observed by rapid-sampling Argo floats (Zhang et al. 2015). Combined with the concurrent temperature/salinity and velocity measurements from mooring arrays, the dynamic characteristics of these two types of SCVs have been described in detail by Zhu et al. (2021). Their results show that the warm-core SCVs exhibit larger volumes and higher swirl speeds but weaker anomalies in hydrographic signals than cold-core SCVs.

Water mass analysis suggests that Kiddies between 26.2 and 26.7 σ_0 most likely form at the subarctic front through subduction in the wintertime (Spall 1995; Zhang et al. 2015; Li et al. 2017), while the warm-core SCVs below the mixed layer could be generated by topography friction along the southern coast of Japan (Zhu et al. 2021). However, the above discussion is derived under the assumption that their water properties are conserved during propagation, leaving details of generation processes unexplored.

Here, we combine in situ observations and high-resolution model simulations to investigate the properties and early life cycle of SCVs in the KOE region. The results show that most SCVs originate from typical topography where friction plays an important role in vortex generation. The rest of this article is organized as follows. Section 2 introduces the mooring data, ocean model configuration and SCV detection method. The model evaluation and SCV properties (e.g., size, velocity, and force balance) are presented in section 3, followed by a discussion on the life cycle of SCV including generation and propagation in section 4. This paper ends with a summary and discussion in section 5.

2. Data and method

a. Mooring data

In 2014, the first subsurface mooring, a part of the Kuroshio Extension Mooring System (KEMS; <https://cn-kems.net>), was deployed in the vicinity of Kuroshio Extension (KE) axis east of Japan (Fig. 1a). After the last cruise in July 2022, the system had included five subsurface moorings (M1, M2, M3, M4, and M5) spanning from 32.4° to 41°N at a water depth of ~5000 m (see Table 1 for details). These moorings carry a series of conductivity–temperature–depth sensors (CTDs; SBE 37-SM), temperature loggers (SBE 56), 75-kHz acoustic Doppler current meters (ADCPs; RDI Workhorse Long Ranger), and deep current meters (CMs; Aquadopp-DW/Seaguard-RCM) to monitor the temporal evolution of in situ temperature, salinity, and current (Fig. 1b).

To the south of the KE axis, the first mooring M1 has been maintained for almost 7 years, and three SCV events were analyzed in detail by Zhu et al. (2021). To the northeast of M1, M3 is located on the KE axis and frequently captures SCVs above 1500 m, while others (M2, M4, and M5) have detected weak or no SCV signals. Therefore, the M3 data in the upper 1500 m are used for analysis in this study. Mooring specifications and data quality control can be found in Zhu et al. (2021). Due to the special position of M3, the strong KE jet often blows down the main float with a maximum drop of 1200 m. This leads to frequent data blanks at the top and only approximately 60% of the data are available. To distinguish the signals between the surface mesoscale eddies and SCVs, the contemporaneous 1/4° daily surface geostrophic velocity derived from Archiving, Validation, and Interpretation of Satellite Data in Oceanography (AVISO) in the KOE region (25°–45°N, 135°–165°E) is also used.

b. ROMS output

To describe the characteristics and associated dynamics of the SCVs, model simulations of the KOE region are conducted

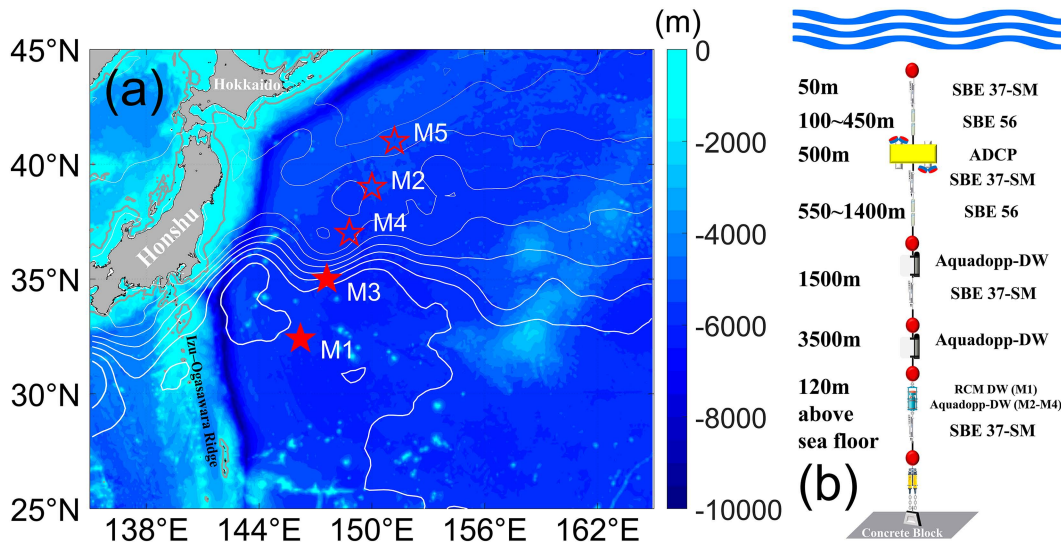


FIG. 1. (a) Locations of the KEMS subsurface moorings. White contours are the mean sea surface height (SSH) between 2015 and 2022; the 600-m isobath is shown in gray. (b) Design schematic of the moorings.

based on the Regional Oceanic Modeling System (ROMS; Shepetchkin and McWilliams 2005). It solves the free surface, hydrostatic and primitive equations for the velocity, temperature, and salinity using a full equation of state for seawater, and it has been successfully applied to investigate SCVs in many regions (e.g., Molemaker et al. 2015; Vic et al. 2015; Gula et al. 2019). In this study, a 1-yr simulation for the KOE region (28°–43.5°N, 138°–162°E) with a resolution of ~1.5 km is nested from a parent model covering the northwest Pacific Ocean (10°S–45°N, 95°–170°E) with a coarser resolution of ~7.5 km. The parent model is spun up for twenty years to reach a statistically equilibrated state and then run for another year to provide the daily boundary information for the nested child simulation. In the vertical direction, 60 topography-following levels with a stretching grid at the bottom can well resolve the flows over complex terrain. The bathymetry is constructed based on the 1/120° General Bathymetric Chart of the Oceans (GEBCO) dataset produced by the British Oceanographic Data Centre (BODC). Due to the computation restriction for the steepness and roughness of the topography, the topography is locally smoothed where the steepness exceeds 0.2. The effect of bottom friction is parameterized through a logarithmic law of the wall above the bottom roughness. The *K*-profile parameterization vertical mixing scheme is adopted to parameterize subgrid-scale vertical mixing processes (Large et al. 1994). A neutral biharmonic mixing operator is utilized for horizontal mixing of tracers (Lemarié et al. 2012).

All surface atmospheric and lateral oceanic forcing are climatological. Both simulations are forced at the surface by the daily mean climatology of the Quick Scatterometer (QuikSCAT) wind stress dataset. Heat and freshwater atmospheric forcing are derived from the monthly climatology of the International Comprehensive Ocean–Atmosphere Dataset (ICOADS) (Woodruff et al. 2011; Freeman et al. 2017). The boundary conditions of the parent model are taken from the monthly climatology of the Simple Ocean Data Assimilation (SODA) reanalysis dataset (Carton and Giese 2008). More details about the model setup can be found in Cao et al. (2021) and Jing et al. (2021). Based on previous studies, simulations have shown good performance in characterizing the circulation, thermohaline structure, mesoscale eddies and submesoscale motions in the KOE region (Luo et al. 2020; Cao and Jing 2022; Dong et al. 2022). In this study, we will use the temperature, salinity, density, and velocities in the upper 2000 m from the model output.

c. SCV detection method

The Okubo–Weiss (OW) method is applied for SCV detection here, which has been widely used in previous studies to identify surface and subsurface eddies (e.g., Kurian et al. 2011; Xu et al. 2019). The OW parameter *W* (Okubo 1970; Weiss 1991) is defined as

$$W = s_n^2 + s_s^2 - \zeta^2, \tag{1}$$

TABLE 1. Mooring positions and deployment date.

| Mooring | Latitude | Longitude | First deployment date | Water depth (m) |
|---------|----------|-----------|-----------------------|-----------------|
| M1 | 32.4°N | 146.2°E | November 2015 | 6002 |
| M2 | 39.0°N | 150.0°E | April 2016 | 5399 |
| M3 | 35.0°N | 147.6°E | October 2017 | 5852 |
| M4 | 37.0°N | 148.8°E | November 2019 | 5832 |
| M5 | 41.0°N | 151.2°E | May 2021 | 5015 |

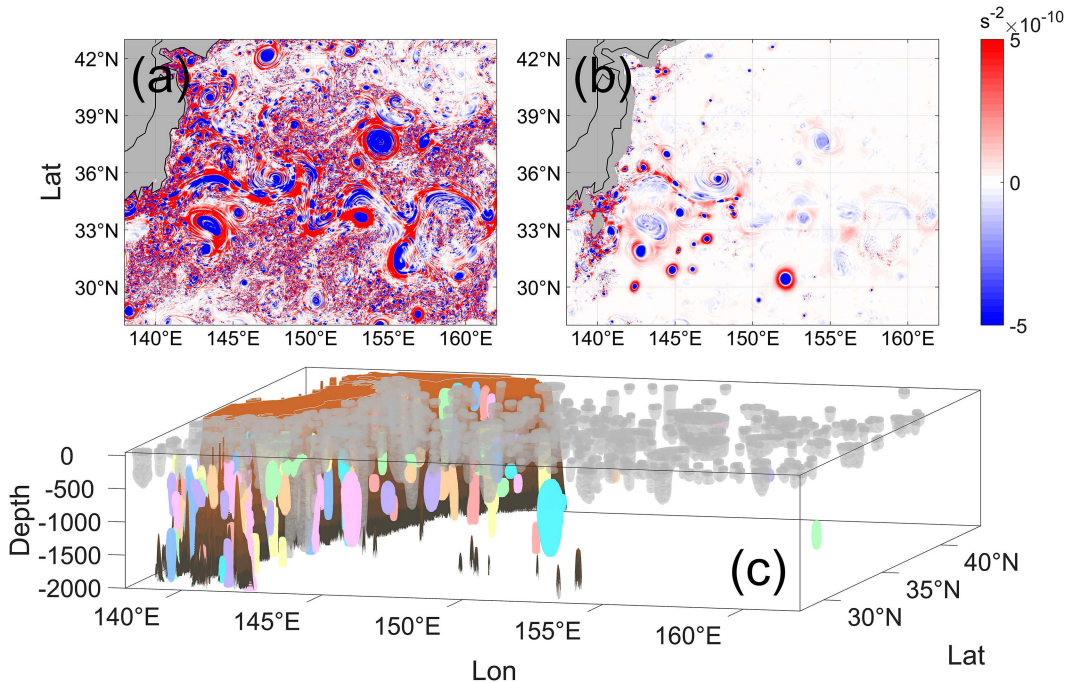


FIG. 2. The W field at (a) the surface and (b) 600-m depth. (c) Identified three-dimensional regions for SCVs (colored shading) and surface eddies (gray shading).

where $s_n = \partial u/\partial x - \partial v/\partial y$ and $s_s = \partial v/\partial x + \partial u/\partial y$ are the normal and shear components of strain, respectively, and $\zeta = \partial v/\partial x - \partial u/\partial y$ is the relative vorticity. This parameter computes the relative dominance of strain and vorticity, which allows us to separate the flow into three regions: the vorticity-dominant region ($W < -W_0$), the shear-dominant region ($W > W_0$) and the background field ($|W| \leq W_0$). In general, vortices have a vorticity-dominant inner region surrounded by a shear-dominant region (Figs. 2a,b), and their edges can be identified with a closed contour corresponding to $W = -W_0$.

To reduce the noise in the SCV detection, the W field is first spatially smoothed with a boxcar filter of $0.1^\circ \times 0.1^\circ$ to search for vortex regions with $W \leq -W_0$ at each depth level. It is noted that the threshold W_0 in the entire domain is set to a constant 5×10^{-9} to avoid vortex signals disappearing at certain levels. Other thresholds are also tested for SCV detection and the results are found to be insensitive to the choice of W_0 value. Based on Kurian et al. (2011), an eddy shape test is introduced to calculate the shape error between each detected region and a circle of equal area. In this study, a region with a shape error of less than 60% is considered a vortex. The small structures with fewer than 4 grid points in the zonal or meridional direction are excluded as they may not be resolved in our model simulation. To obtain the three-dimensional structure of the SCV, these vortex regions at every two adjacent depth levels are double-checked and the vertically overlapping regions are labeled as the same vortex. All surface eddies with their tops at the surface (gray shadings in Fig. 2c) are removed in the following analysis. Some associated definitions of SCV properties are listed below: the vortex center (C_x, C_y, C_z) is

defined to be the geometrical center of the three-dimensional detected region; the radius (R) is defined as that of the circle with an area equal to the largest horizontal region within the vortex; the thickness (H) is defined by the vertical extent between the top and bottom; and the polarity is defined as the sign of ζ at the center.

After identifying the SCVs in the entire time series, their trajectories can be determined at different depth levels by an automated tracking procedure. For each SCV at time step k , we compare its vortex properties with those of the SCVs at time step $k + 1$. The property differences between a vortex pair in terms of depth, radius and thickness are given by $|C_z^{k+1} - C_z^k|/C_z^k$, $|R^{k+1} - R^k|/R^k$, and $|H^{k+1} - H^k|/H^k$, respectively. Assumed that the SCV evolves slowly over time, it can be tracked by finding the nearest center at $k + 1$ with property differences smaller than 60% in a search radius of 0.5° . Cyclones and anticyclones are treated separately. The split and merged SCVs are considered as new vortices because their properties change too much.

d. SCV swirl velocity

SCVs are usually advected by the background circulation with a swirl speed comparable to the background velocity (McWilliams 1985), leading to an offset in the eddy horizontal velocity distribution in the Eulerian grid (Lilly and Rhines 2002). To better describe the eddy velocity (u, v) under a uniform background flow $\mathbf{U}_b = (u_b, v_b)$, a Rankine vortex model is used here. It consists of an inner core in solid rotation with an irrotational vortex in the far field, which can be expressed in terms of the Cartesian coordinate system as

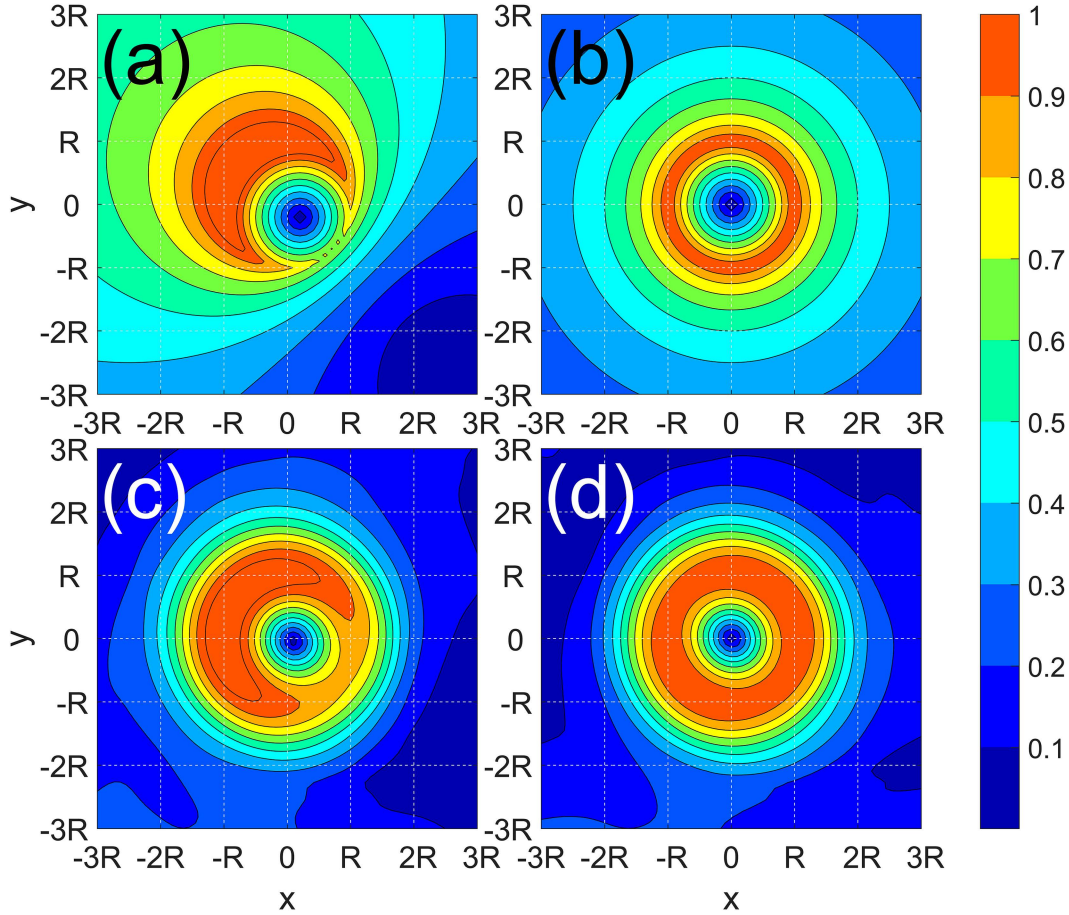


FIG. 3. Horizontal velocity distribution of the Rankine vortex model containing (a) background flow and (b) no background flow. (c),(d) As in (a) and (b), but for a simulated SCV in the ROMS output.

$$\begin{cases} u = \frac{V_{\max}}{R}y + u_b, \\ v = -\frac{V_{\max}}{R}x + v_b, \end{cases} \text{ for } \sqrt{x^2 + y^2} \leq R, \text{ and} \quad (2)$$

$$\begin{cases} u = V_{\max}R \frac{y}{x^2 + y^2} + u_b, \\ v = -V_{\max}R \frac{x}{x^2 + y^2} + v_b, \end{cases} \text{ for } \sqrt{x^2 + y^2} > R, \quad (3)$$

where (x, y) is the point referenced to the vortex center and V_{\max} is the maximum azimuthal velocity at R . Figures 3a and 3b show the velocity magnitude field when $u_b = v_b = 0.2V_{\max}$ and $u_b = v_b = 0$, respectively. With the influence of background flow, the zero-velocity point is shifted toward the lower right, resulting in a “false” vortex center. The velocity of the SCV is also influenced by the background flow, which depicts a crescent-shaped distribution in the upper left. Similar offset phenomena would be observed if using other vortex models such as the Gaussian model and Taylor model (figures not shown). By examining the velocity fields of SCVs derived from ROMS output, it is found that this nonaxisymmetric structure bias is very common (Fig. 3c). To separate the vortex swirl velocity (\mathbf{U}_S) and

\mathbf{U}_b from the total velocity \mathbf{U} , we assume that the \mathbf{U}_S distribution is axisymmetric and \mathbf{U}_b is uniform in the vortex core. The integral of \mathbf{U} per unit volume for the entire SCV yields \mathbf{U}_b :

$$\frac{\iiint_{\Omega} \mathbf{U}(x, y, z) dv}{\iiint_{\Omega} dv} = \frac{\iiint_{\Omega} \mathbf{U}_S(x, y, z) dv}{\iiint_{\Omega} dv} + \frac{\iiint_{\Omega} \mathbf{U}_b(x, y, z) dv}{\iiint_{\Omega} dv} = \mathbf{U}_b, \text{ for } (x, y, z) \in \Omega, \quad (4)$$

where Ω is the three-dimensional region identified by the OW method. Then, \mathbf{U}_S can be obtained by subtracting \mathbf{U}_b from \mathbf{U} . Figure 3d shows the \mathbf{U}_S distribution of the original velocity field in Fig. 3c after \mathbf{U}_b is removed. The zero of velocity is located at the SCV center and the crescent-shaped distribution disappears, which suggests that the effect of background flow has been eliminated.

3. Statistical analysis

a. Validation of ROMS simulation

Before analyzing the ROMS output, it is necessary to verify whether the model can reproduce the characteristics of SCVs.

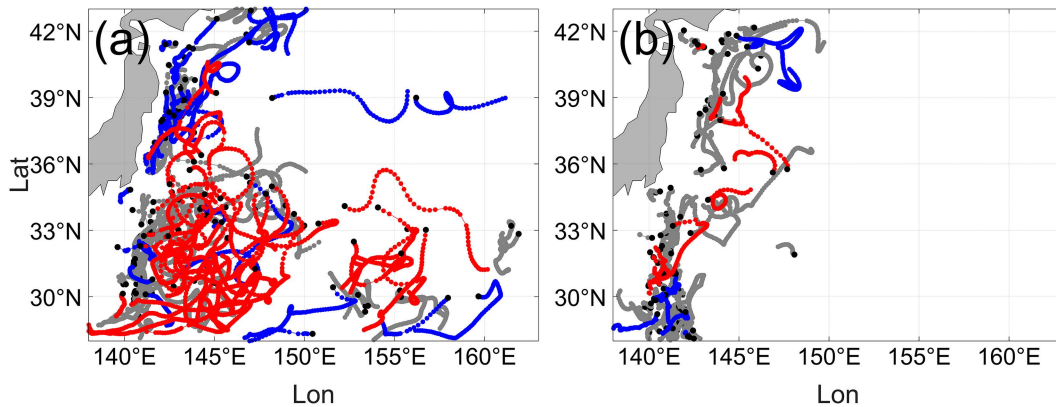


FIG. 4. Trajectories of simulated (a) anticyclonic and (b) cyclonic SCVs. Red (blue) dots represent the warm-core (cold-core) SCVs. Black dots show the first detection locations.

According to the SCV detection procedure (section 2c), a total of 13514 vortices are identified and 260 trajectories with vortex life longer than 30 days are tracked in the 1-yr simulations (Fig. 4). The ratio of anticyclones to cyclones is approximately 3:2, and the average lifetime of anticyclones is 10 days longer than that of cyclones. This polarity asymmetry is associated with stronger strain-induced vortex weakening in cyclones than in anticyclones (Graves et al. 2006), which is consistent with the results in observational and numerical studies (e.g., Collins et al. 2013; Molemaker et al. 2015). Compared to anticyclonic SCVs, cyclonic SCVs are found to be concentrated near the continental shelf of Japan and travel shorter distances in the zonal direction (Fig. 4b), implying that they contribute less to water mass transport in the subsurface layer. Therefore, we focus mainly on anticyclonic SCVs in the following, while a preliminary analysis of cyclonic SCVs can be found in the online supplemental material.

To estimate whether the vortex has a warm or cold core, we interpolate the θ/S field onto isopycnals from $24.0\sigma_0$ to $28.0\sigma_0$ with an interval of $0.05\sigma_0$ and calculate the temperature/salinity anomalies (θ_a/S_a) by subtracting the background θ/S profiles, which are defined as the averaged θ/S at each isopycnal over surrounding waters from $2R$ to $3R$. Following Li et al. (2017) and Zhu et al. (2021), a warm-core (cold-core) vortex is identified when a positive (negative) S_a with a value exceeding 0.05 at the center is detected. In total, 35 cold-core SCVs are detected, and most of them move along the continental shelf of Honshu and Hokkaido, Japan (blue dots in Fig. 4a). The distribution of hydrographic properties shows that most of their cores exist between the $26.8\sigma_0$ and $27.3\sigma_0$ isopycnals, with θ and S values of $2^\circ\text{--}5^\circ\text{C}$ and 33.9–34.3 psu, respectively (Figs. 5a–c). The average R is about 9 ± 2 km, smaller than the first baroclinic deformation radius of 30–40 km estimated by Chelton et al. (1998) in the KOE region. The average H and V_{\max} are 610 ± 350 m and 0.20 ± 0.08 m s^{-1} , respectively (Figs. 5d–f). In addition, 31 warm-core SCVs are identified at lower latitudes, and they are mainly trapped in the southern recirculation gyre (red dots in Fig. 4a) without obvious preference for drift direction. Their cores are concentrated

between the 26.2 and $27.0\sigma_0$ isopycnals, with typical θ and S values ranging from 6° to 12°C and from 34.3 to 34.5 psu, respectively. Compared to the cold-core counterparts, the warm-core SCVs are characterized by large horizontal scales and high kinetic energy, with an average R of 15 ± 7 km and an average V_{\max} of 0.35 ± 0.18 m s^{-1} . The histogram shows that the warm-core vortices have a thickness comparable to that of cold-core vortices, with an average value of 550 ± 370 m (Fig. 5e). The results closely match the statistical analysis of the “spicy” (warm and salty) and “minty” (cold and fresh) SCVs in the KOE region derived from Argo float data (McCoy et al. 2020), indicating that anticyclonic SCVs can be reasonably simulated by ROMS.

In addition to the statistical characteristics, the robustness of the ROMS output is further validated by mooring data. During the 5-yr-long observation period, mooring M3 captured a total of eleven SCVs in the upper 1500 m (see Table 2 for details), and these SCVs exhibit the common dynamic characteristics described in Zhu et al. (2021). Given the strong background currents, it is most likely that these SCV signals were associated with multiple vortices rather than from repeated observations of the same vortex. The largest SCV passed M3 in September 2020 at 700-m depth, with a thickness of about 600 m and a maximum velocity of 0.44 m s^{-1} (Figs. 6a–c). A clear southward-to-northward velocity pattern with a lens of relatively homogeneous water at the depth of the velocity core indicates that it is an anticyclonic vortex. The frequent appearance of SCVs at M3 implies that the Kuroshio current may be an important pathway for SCVs into the ocean interior. For comparison, we extract 1-yr velocity and temperature profiles at the same location of M3 in the simulations. Based on the vortex detection results, it is found that three warm-core SCVs pass the site on 30 June, 6 July, and 20 November. Although the timing of the SCV passages does not match the mooring observations, the simulated SCVs exhibit a similar dynamic structure to the observed ones, with comparable vertical extents and kinetic energies ($H = 700$ m and $V_{\max} = 0.47$ m s^{-1} ; see Figs. 6d–f). Next, we describe the dynamic characteristics of anticyclonic SCVs based on composition analysis.

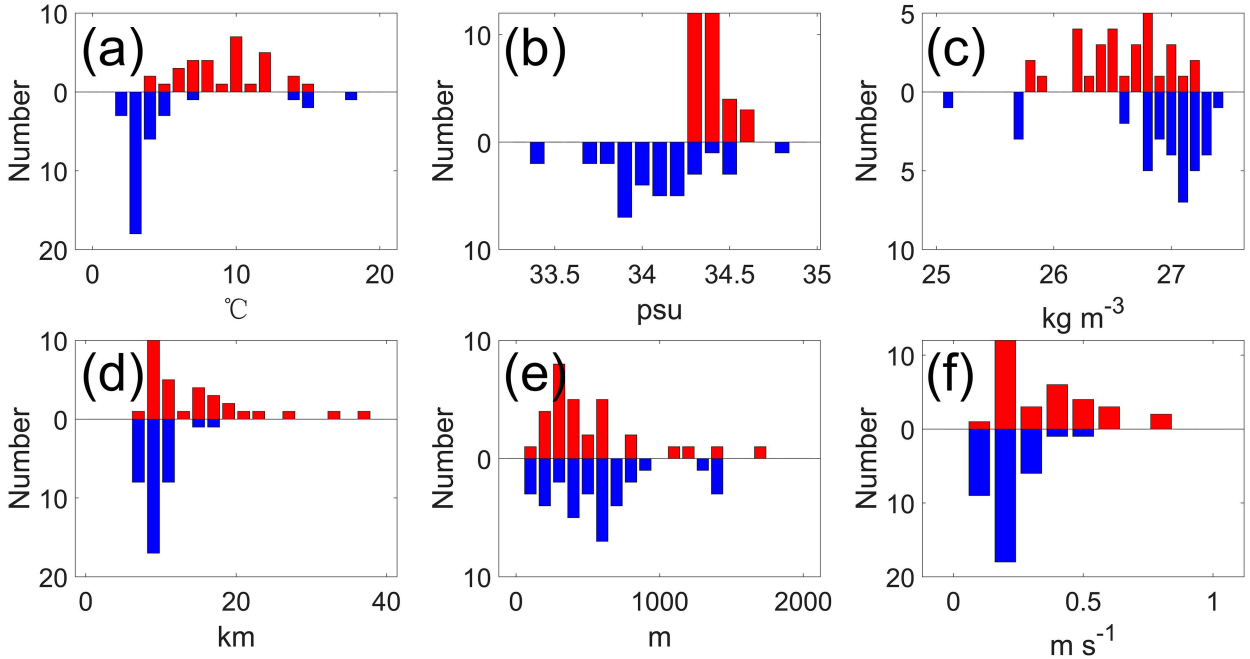


FIG. 5. Histograms of SCV (a) core temperature θ , (b) core salinity S , (c) core density, (d) radius R , (e) thickness H , and (f) maximum swirl velocity V_{max} . Red (blue) bars show warm-core (cold-core) SCV distributions.

b. Dynamic characteristics

To study the spatial structure and force balance inside an SCV, the pressure fields (P) are obtained by integrating the density profiles vertically from the sea surface under the hydrostatic equilibrium condition. Similar to the definitions of θ_d/S_a , the pressure/potential density anomalies (P_d/σ_a) relative to the background profiles averaged from $2R$ to $3R$ are calculated. For each identified SCV, all variables in the region centered at (C_x, C_y, C_z) from $-5R$ to $5R$ and from $-H$ to H are normalized by their maximum values. The composite $|\theta_a|$ for all warm-core and cold-core anticyclones shows that the vortex wraps the anomalous water mass within $2R$ and contains a fairly homogeneous core with a radius of $0.5R$ (Fig. 7a).

TABLE 2. SCVs observed by mooring M3 between October 2017 and June 2022; H and V_{max} are the thickness and the maximum swirl velocity, respectively.

| No. | Date | Elapsed time (h) | H (m) | V_{max} (m s^{-1}) |
|-----|----------------|------------------|---------|--|
| 1 | May 2018 | 68 | 470 | 0.38 |
| 2 | July 2019 | 61 | 350 | 0.26 |
| 3 | August 2020 | 90 | 340 | 0.37 |
| 4 | September 2020 | 68 | 330 | 0.22 |
| 5 | September 2020 | 141 | 580 | 0.44 |
| 6 | October 2020 | 43 | 250 | 0.32 |
| 7 | January 2021 | 58 | 270 | 0.22 |
| 8 | April 2021 | 61 | 490 | 0.28 |
| 9 | September 2021 | 90 | 380 | 0.43 |
| 10 | October 2021 | 93 | 390 | 0.42 |
| 11 | November 2021 | 104 | 440 | 0.36 |

Above (below) the vortex core, the isopycnals are domed (depressed) with the largest deformation at $\pm 0.5H$, which corresponds to a positive P_a inside the SCV (Fig. 7b). Zhang et al. (2017) proposed that the three-dimensional structure of subsurface eddies has separable vertical and horizontal components $P_a(h, r) = F_v(h)F_h(r)$, where F_v and F_h are the vertical and horizontal structure functions of cylindrical coordinates (h, r) normalized by H and R , respectively. Figure 8a shows that F_v can be well fitted by a cosine function plus a constant value, which is consistent with the approximate solution from the quasigeostrophic equation (Zhang et al. 2017). However, the horizontal force balance in such small-scale vortices is ageostrophic and the centrifugal force needs to be considered (e.g., McWilliams 1985; Bosse et al. 2017). Therefore, we examine the gradient wind balance in the cylindrical coordinate system, which can be expressed as

$$f|\mathbf{U}_S| = -\frac{1}{\rho_0 R} \frac{\partial P_a}{\partial r} + \frac{|\mathbf{U}_S|^2}{rR}, \tag{5}$$

where f is the Coriolis parameter and ρ_0 is the reference seawater density. Physically, the equation describes the balance between the Coriolis force (CF), pressure gradient force (PF), and centrifugal force (CE). As shown in Fig. 8b, the inward CF is well balanced with the outward PF and CE, indicating that the force balance of the SCV satisfies the gradient wind rather than the geostrophic balance. The Rossby number (Ro), the ratio of CE to CF, ranges from 0.25 to 0.4 within the vortex core. This means that neglecting CE would underestimate $|\mathbf{U}_S|$ by 25%–40%, consistent with the mooring observations of an anticyclonic SCV in the South China Sea (Zhang et al. 2022).

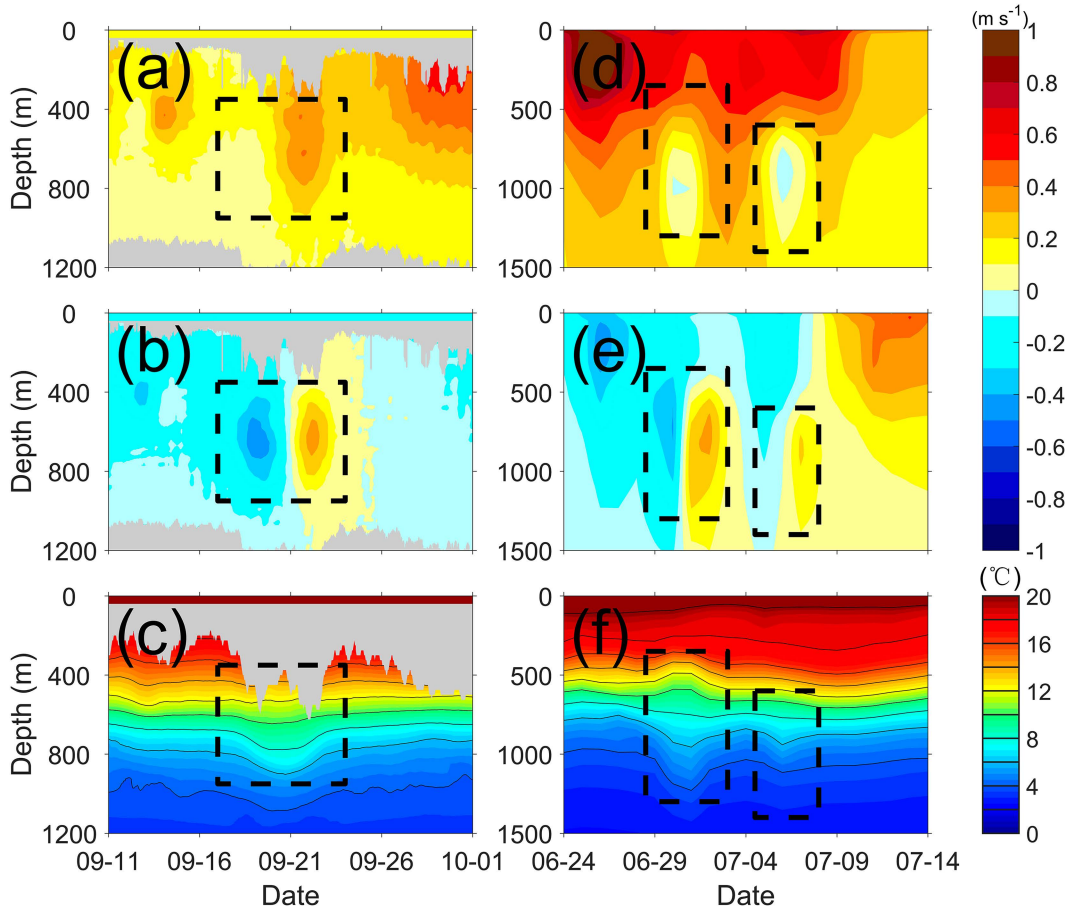


FIG. 6. Depth–time plots of (a) zonal velocity, (b) meridional velocity, and (c) temperature from M3 in September 2020. The surface geostrophic currents in (a) and (b) and surface temperature in (c) are derived from satellite data. (d)–(f) As in (a)–(c), but for the location of M3 in the ROMS output. Dashed boxes denote the SCV locations.

It is also shown that CF and PF share a similar radial structure, but the peak position of PF is more outward due to the presence of CE (Fig. 8b). According to Wang et al. (2015) and Yang et al. (2019), the Taylor vortex model is a reasonable approximation for ocean eddies and its tangential velocity can be written as

$$u_{\theta}(r) = ar \exp(-br^2), \quad (6)$$

where a and b are fitting parameters. Performing a simple linear least squares fit to the composite \mathbf{U}_s/V_{\max} reveals that the radial structure of SCVs can be well represented by the Taylor vortex model with $a = 1.44$ and $b = 0.38$. Combining Eq. (5) with Eq. (6) yields an equation for the dimensionless pressure gradient:

$$\begin{aligned} \frac{P_0}{\rho_0 f R V_{\max}} \frac{\partial p(r)}{\partial r} &= u_{\theta}(r) - \frac{V_{\max} u_{\theta}^2(r)}{fR} \\ &= ar \exp(-br^2) - \text{Ro} a^2 r \exp(-2br^2), \end{aligned} \quad (7)$$

where P_0 is the scale of the SCV-induced pressure anomaly. For mesoscale eddies ($\text{Ro} \sim 0$), the velocity and pressure

gradient are described by the same radial structure. With decreasing horizontal scale, the CE becomes more important in the SCVs, which shifts the peak of the pressure gradient to the vortex edge.

Compared to the horizontal velocities, our knowledge about the vertical motion of SCVs is more limited because it requires three-dimensional high-resolution measurements of vertical velocity (w) fields, which is difficult to achieve in field observations. In this regard, the high-resolution model is a useful tool for understanding the structure of the w field. Most simulated SCVs have a dipole pattern that consists of an upwelling cell and a downwelling cell on both flanks of the vortex, which has also been reported in the diagnosed w field of a subtropical SCV (Barceló-Llull et al. 2017). Prior to compositing, the w field for each SCV is rotated horizontally so that the positive (negative) w is in the $y > 0$ (< 0) region. As shown in Figs. 7c and 7d, w is zero between two cells and reaches a maximum at the vortex edge, about 50 m day^{-1} , and the upward motion can favor nutrient fluxes into the euphotic layer and enhance local primary production.

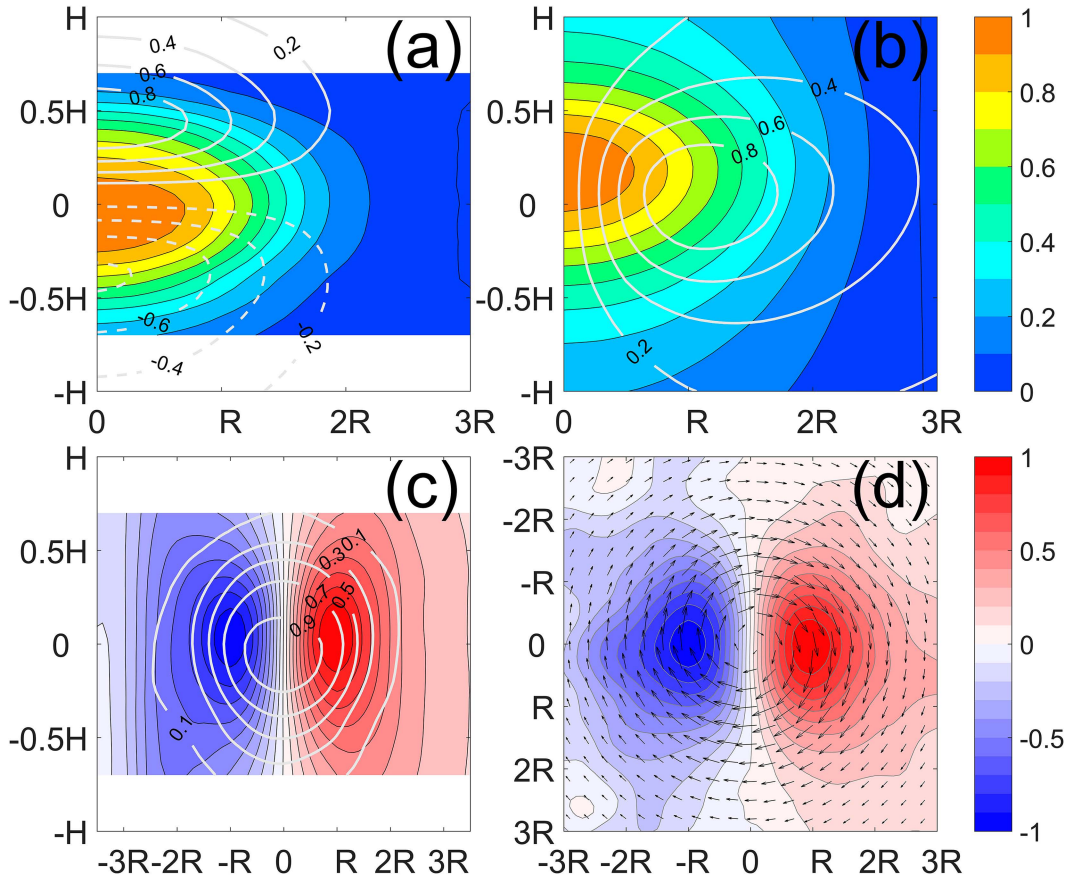


FIG. 7. Radial distribution of (a) temperature anomaly $|\theta_a|$ and (b) pressure anomaly P_a from composite anticyclonic SCVs. (c) Vertical and (d) horizontal sections of composite vertical velocity w across the vortex center. White contours show the density anomaly in (a), velocity magnitude in (b), and $|\theta_a|$ in (c). Arrows in (d) are SCV swirl velocity vectors.

4. Generation and propagation

In this section, we describe the early life cycle of SCVs in the KOE region, including the generation and propagation processes. Some effort has been made to track SCVs in observations. The Lagrangian platform, such as the neutral density float RAFOS, can keep track of SCVs for hundreds of days and has been deployed in the northeastern Pacific Ocean and northeastern Atlantic Ocean to study the early evolution of Meddies and Cuddies (Collins et al. 2013; Bashmachnikov et al. 2015). In combination with shipboard surveys, a Meddy was relocated and resampled four times over a 2-yr period, documenting the significant changes in its structure and water properties (Armi et al. 1989; Hebert et al. 1990). However, the lack of such multiplatform observational studies in the KOE region limits our understanding of the generation mechanism and evolution of different types of SCVs. Since the statistical results demonstrate that the high-resolution simulations can largely reproduce the characteristics of SCVs in this region, we use them to explore the life cycle of SCVs in the following.

Typically, the strong negative relative vorticity and weak stratification in the SCVs lead to low potential

vorticity (PV) anomalies compared to the background fields (McWilliams 1985). PV is defined as the dot product of the absolute vorticity $\omega_a = f\mathbf{z} + \nabla \times \mathbf{u}$ and the buoyancy gradient $\nabla b = -g\nabla\sigma/\rho_0$, where \mathbf{z} is the unit vertical vector, g is the gravitational acceleration, and σ is the potential density referenced to the surface. According to the impermeability theorem (Haynes and McIntyre 1987), there is no PV flux across an isopycnal surface, and PV can neither be created nor destroyed within a layer bounded by two isopycnal surfaces except at boundaries with strong nonconservative or diabatic processes, such as deep convection and wind-driven friction at the surface (Testor and Gascard 2006; Thomas 2008; Bosse et al. 2016) or bottom friction and mixing near the bottom topography (McWilliams 1985; D’Asaro 1988). As such, we can locate the formation sites of SCVs by tracking the trajectory of PV signals.

The core θ/S distributions of the SCVs captured by mooring M1 suggest that their origin can be traced back to the eastern and southern coasts of Japan (see Fig. 14 in Zhu et al. 2021). As shown in Fig. 4, most SCV trajectories originate near the continental slope east of Japan over the entire domain. Their core density mainly ranges from 26.2 to $27.3\sigma_0$, and these

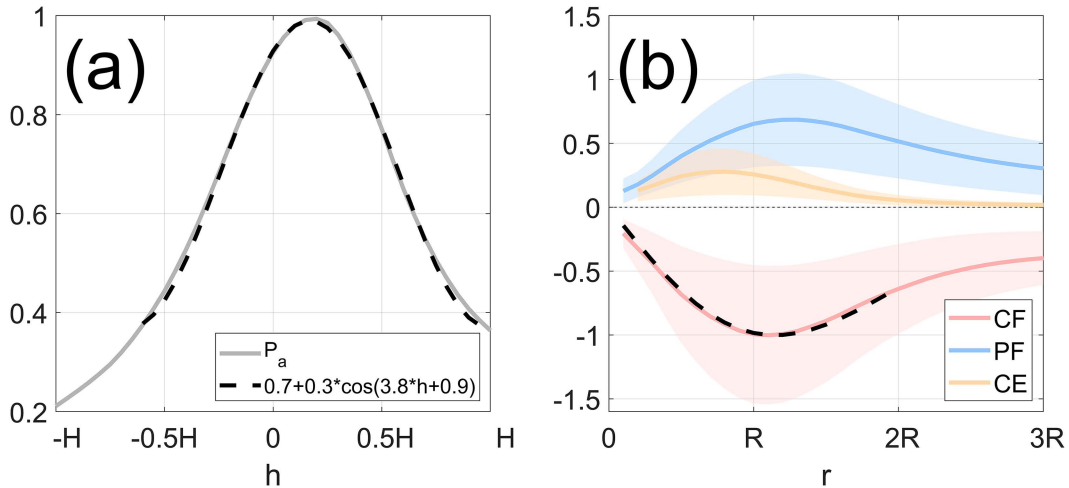


FIG. 8. (a) Vertical distribution of the normalized pressure anomaly P_a through the vortex center. (b) Radial distribution of the normalized Coriolis force CF, pressure gradient force PF, and centrifugal force CE of anticyclonic SCVs. The dashed lines are the fitted cosine function in (a) and the fitted Taylor vortex model in (b). The shading represents the standard deviations.

isopycnals intersect the bottom along the continental slope but do not crop out at the surface. This indicates that the SCVs are most likely generated through flow–topography interactions rather than surface processes. To give a more precise description of the dynamic processes near the continental slope, we plot snapshots of ζ at 600-m depth offshore of Honshu and Hokkaido Island in Fig. 9. It is found that the Izu–Ogasawara Ridge along 140°E is a key region for vortices and filaments with horizontal scales of $O(1\text{--}10)$ km. The strong Kuroshio flows eastward over it at an average water depth of ~ 450 m at 33°–34°N (Fig. 10a). In the bottom boundary layer, the velocity shear generates negative (positive) ζ in the direction along (against) the Kelvin wave propagation. The time-averaged ζ field over a 1-yr simulation shows that the negative values are dominant in the northern part of the Izu–Ogasawara Ridge with the smallest value of less than $-f$ at 600-m depth (Figs. 10b,c), which causes the PV to become negative and meets a criterion for the ageostrophic centrifugal instability (Hoskins 1974). Subsequently, the negative ζ separates from the northern tip of the ridge (33.9°N, 140°E) that has a large topographic curvature, and forms an anticyclonic SCV after ~ 10 days (Figs. 9a–f). This is similar to the SCV generation process along the eastern seaboard of the United States where the Gulf Stream meets the Charleston Bump (Gula et al. 2019).

To investigate the contribution of topography friction to PV reduction, we use a conservation equation for PV (q), which can be written in flux form:

$$\frac{\partial q}{\partial t} = -\nabla \cdot \left(\underbrace{q\mathbf{u}}_{Q_A} - \underbrace{\boldsymbol{\omega}_a \frac{Db}{Dt}}_{Q_D} + \underbrace{\nabla b \times \mathbf{F}}_{Q_F} \right), \quad (8)$$

where \mathbf{F} represents the nonconservative forces per unit mass (Marshall et al. 2001). The three terms on the right-hand side

represent the advection (Q_A), diabatic flux (Q_D), and frictional flux (Q_F) of the PV. Following Gula et al. (2015), Q_F at the bottom can be computed as the sum of the horizontal (Q_F^h) and vertical (Q_F^v) components:

$$Q_F = \underbrace{\left(\frac{\partial b}{\partial y} F_b^z - \frac{\partial b}{\partial z} F_b^y \right) n_x + \left(\frac{\partial b}{\partial z} F_b^x - \frac{\partial b}{\partial x} F_b^z \right) n_y}_{Q_F^h} + \underbrace{\left(\frac{\partial b}{\partial x} F_b^y - \frac{\partial b}{\partial y} F_b^x \right) n_z}_{Q_F^v}, \quad (9)$$

where $\mathbf{n} = (n_x, n_y, n_z)$ is the unit vector normal to the bottom and $\mathbf{F}_b = (F_b^x, F_b^y, F_b^z)$ is the vertical gradient of stress at the bottom that has an approximation after integrating over the boundary layer depth:

$$\mathbf{F}_b \approx -\frac{C_d |\mathbf{u}_0|}{\rho_0 h_b} \mathbf{u}_0, \quad (10)$$

where C_d is the drag coefficient, \mathbf{u}_0 is the velocity vector at the bottom, and h_b is the depth of the bottom boundary layer. In the vicinity of the northern tip of the Izu–Ogasawara Ridge, the time-averaged Q_F is negative between the 600- and 900-m isobaths, which is mainly contributed by the horizontal frictional flux (Figs. 11a–c). Its magnitude reaches 10^{-11} m s $^{-4}$ and is two orders of magnitude larger than the Q_A (figures not shown), suggesting that the low PV anomalies are generated by topography friction rather than advection from other regions. In a similar way, the Oyashio originating at high latitudes flows southwestward over the topography to its right, with negative ζ values being produced along the continental slope of Hokkaido

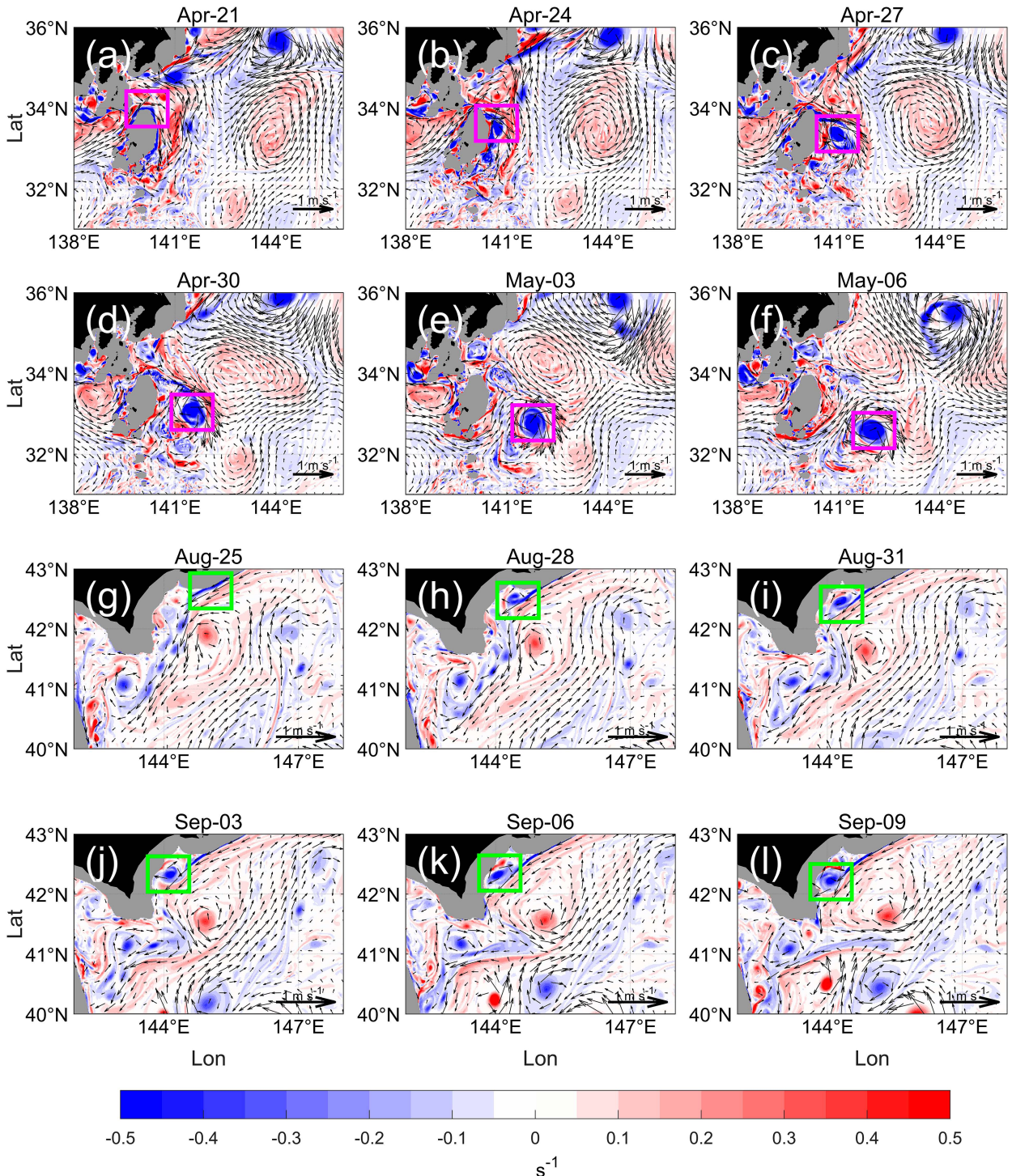


FIG. 9. (a)–(f) Snapshots of relative vorticity ζ/f at 600-m depth around the Izu–Ogasawara Ridge. (g)–(l) As in (a)–(f), but at 300-m depth along the Hokkaido slope. Generation of a warm-core (cold-core) SCV is marked by magenta (green) boxes.

Island (Figs. 9g–l and 10e–f). The ζ minima tend to occur at a shallower layer of ~ 300 m, but the time-average Q_F is of a smaller order (10^{-12} m s $^{-4}$) because the Oyashio Current is weaker than the Kuroshio Current (Figs. 11d–f).

In addition to vorticity, the generation of SCVs can also be estimated in terms of eddy kinetic energy (EKE). The energy source for EKE can be examined by computing the energy conversion terms as follows:

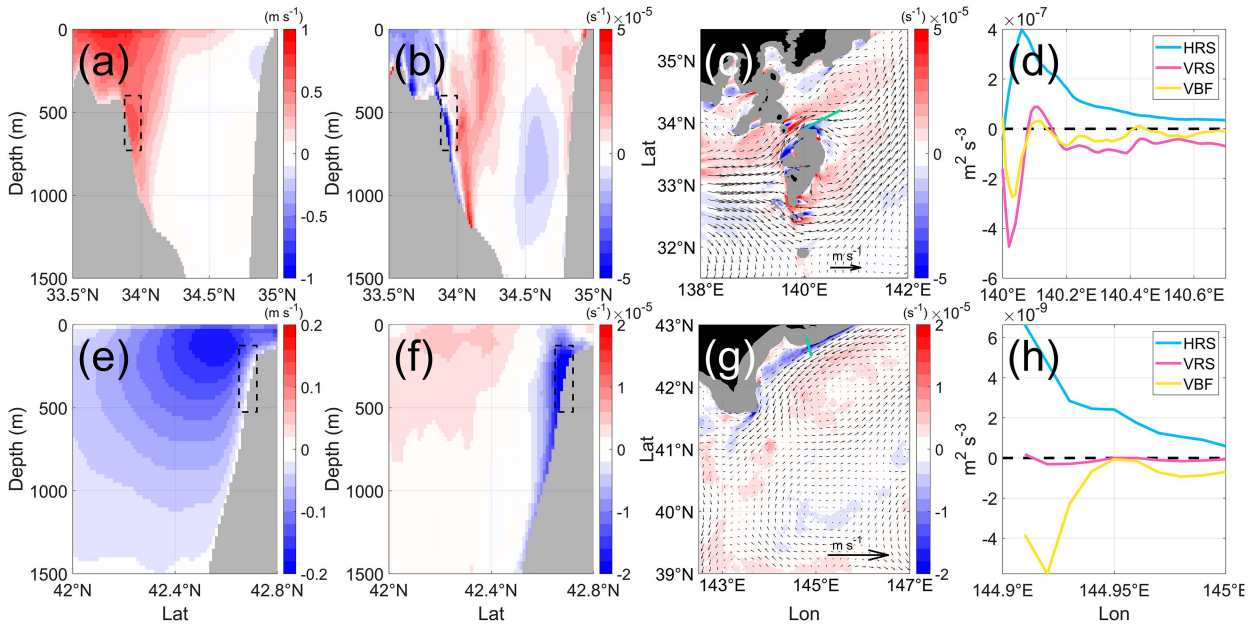


FIG. 10. (a) Mean zonal velocity and (b) relative vorticity ζ of meridional section along 140°E . (e),(f) As in (a) and (b), but for the 145°E meridional section. Black boxes denote the locations where the negative vorticity is generated. Mean ζ field (shadings) and current (arrows) around (c) the Izu–Ogasawara Ridge at 600-m depth and (g) the Hokkaido slope at 300-m depth. (d),(h) Local energy conversions of the HRS, VRS, and VBF along the green lines in (c) and (g), respectively.

$$\begin{cases} \text{HRS} = -\overline{u'u'} \cdot \frac{\partial \bar{u}}{\partial x} - \overline{v'u'} \cdot \frac{\partial \bar{u}}{\partial y} \\ \text{VRS} = -\overline{w'u'} \cdot \frac{\partial \bar{u}}{\partial z} \\ \text{VBF} = -\overline{w'b'} \end{cases}, \quad (11)$$

where the overbar denotes the moving average for 10 days and the prime denotes fluctuations relative to the time average. HRS and VRS are the conversion from mean to eddy kinetic energy due to horizontal and vertical shear, respectively. VBF is the conversion from eddy potential to eddy kinetic energy. Figures 10d and 10h show the vertical integration of these three terms along two cross-stream lines near the Izu–Ogasawara Ridge and Hokkaido Island, respectively. The positive HRS reaches its maximum near the boundary and decays rapidly away from the boundary, whereas the VRS and VBF are primarily negative along the lines. This suggests that the barotropic conversion of kinetic energy from the mean flow to the eddies provides the main energy source. In addition to the above two generation sites, there are other locations along the continental slope with the same topographic features that favor SCV generation at different depths. Although the vortices vary in their sizes and water properties, they share similar generation processes and mechanisms.

After generation in the wake of the Izu–Ogasawara Ridge, the warm-core SCVs are carried by the Kuroshio and move eastward rapidly away from the boundary, resulting in a large number of SCVs distributed along the KE axis (Fig. 2b). This could explain why the SCVs are often observed by M3 when

the KE axis passes through. As shown in Fig. 4a, some vortices detach from the first trough of the meander under the inertial effect and enter the southern recirculation gyre; the rest continue to move eastward with the KE. Most cold-core SCVs propagate along the continental slopes of Honshu and Hokkaido Island, and a few enter the KOE region. To assess the temporal evolution of vortices during propagation, we use an offline particle tracking procedure (Parcels; Delandmeter and van Sebille 2019) to describe the three-dimensional motions of particles in the vortex. The advection of particles is calculated based on the fourth-order Runge–Kutta integration including vertical velocity. In this analysis, 50 000 particles are released into two long-lived SCVs (lifetime over 160 days) originating from the Izu–Ogasawara Ridge and from the continental slope of Hokkaido Island. The release regions are large enough to cover the entire vortices and at a certain distance from the generation site to avoid incorrect particle simulations at the boundary (orange and blue rectangles in Fig. 12a). According to the ratio of the total particle number (N_0) to the volume of the release region (V_0), the trapped water volume of the vortex at time step k (V_k) can be estimated as $V_k/N_k = V_0/N_0$, where N_k is the trapped particle number at k .

Figure 12 presents the trajectories of trapped particles and the temporal evolution of V_k for both SCVs. The particle trajectories are exactly coincident with the OW-based results, but the OW-based tracking of the cold-core SCV is lost between day 45 and day 105 due to the interference of a surface eddy located at 39°N , 156°E . Zhang et al. (2017) found that subsurface eddies may trap and carry more water mass above

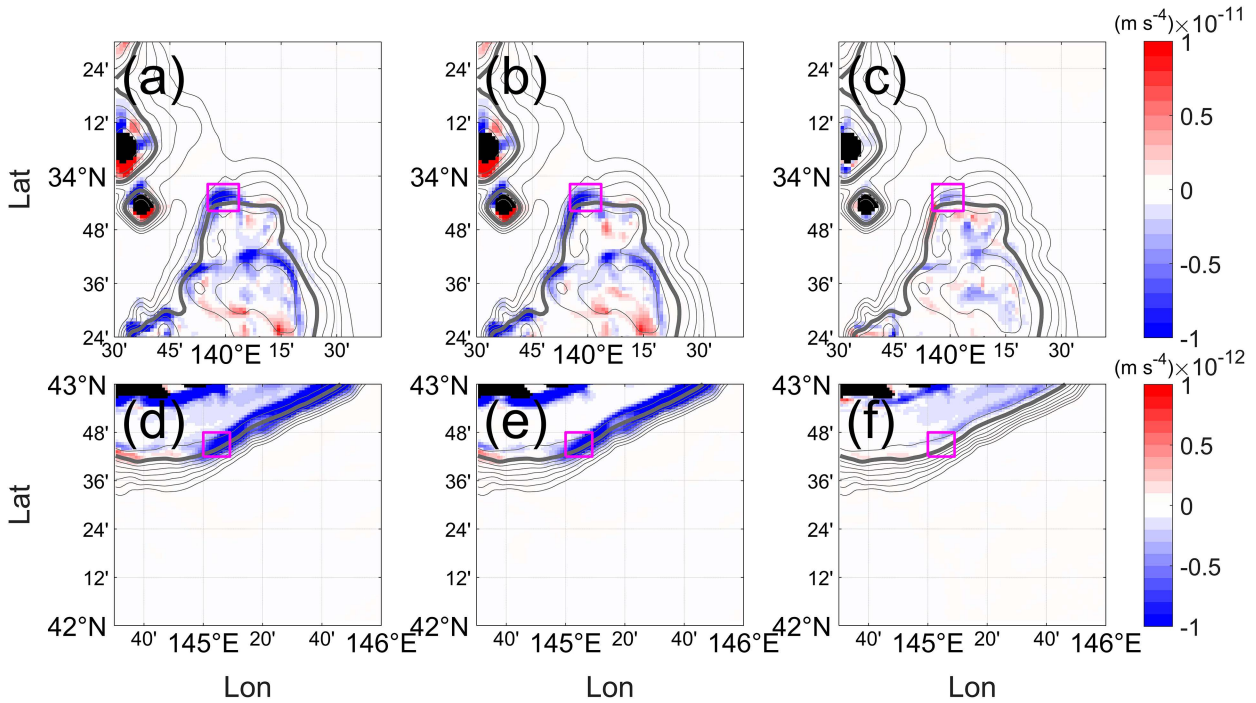


FIG. 11. Time-averaged (a) Q_F , (b) Q_F^h , and (c) Q_F^v around the northern tip of the Izu–Ogasawara Ridge, respectively. (d)–(f) As in (a)–(c), but for the continental slope of Hokkaido Island. Gray lines are isobaths with an interval of 150 m. The thick lines denote 600-m isobath in (a)–(c) and 300-m isobath in (d)–(f). Magenta boxes denote the location where the negative vorticity is generated in Figs. 10b and 10f.

and below the eddy core, accounting for 60% of the total water volume. When the changes in N_k level off after 50 days, the V_k of the warm-core (cold-core) SCV reaches $4.5 \times 10^{11} \text{ m}^3$ ($0.6 \times 10^{11} \text{ m}^3$), which is approximately twice the volume of the velocity core described in section 2c (dashed lines in Figs. 12b,c). Meanwhile, the low reduction rate of V_k , on the order of $10^8 \text{ m}^3 \text{ day}^{-1}$, indicates that the vortices can survive

for several years and play an essential role in water mass transport over long distances.

5. Summary

In this study, the SCVs in the KOE region are investigated with observations and high-resolution model simulations.

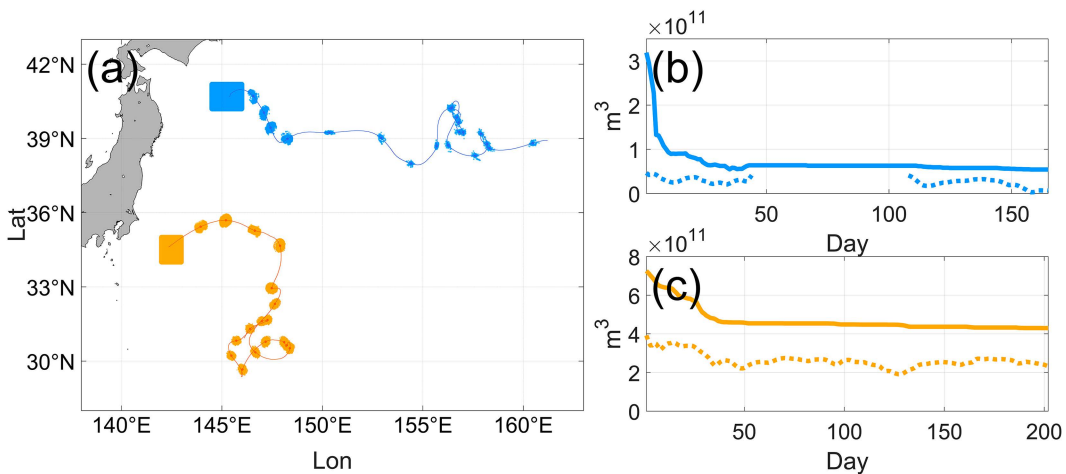


FIG. 12. (a) Trajectories of trapped particles in a warm-core SCV (orange dots) and a cold-core SCV (blue dots). Rectangles indicate the particle release regions. (b),(c) The temporal evolution of trapped water volume V_k for the cold-core SCV and the warm-core SCV, respectively. The dashed lines denote the volume of the vortex core identified by the OW-based method.

Using the OW-based detection and tracking algorithms, 260 vortex trajectories with lives longer than 30 days are obtained from the 1-yr simulation, and more anticyclones than cyclones are detected. The warm-core and cold-core SCVs are similar in number, but the former have larger radii and faster swirl velocities. Statistical analysis further shows that their water properties are very similar to the observational results. Dynamically, SCVs satisfy the gradient wind balance in the horizontal direction with Rossby numbers between 0.25 and 0.4. Based on the Taylor vortex model, we fit the horizontal velocity distribution and deduce the radial structure of the pressure gradient corrected by the centrifugal force. In the vertical direction, the vertical velocity is characterized by a dipolar pattern with maximum values ($\sim 50 \text{ m day}^{-1}$) at the vortex edge. These SCVs are mainly generated on the eastern continental slope of Japan through flow–topography interactions. The Izu–Ogasawara Ridge and slope of Hokkaido are two important generation regions where the Kuroshio Current and Oyashio Current interact with the steep topography through barotropic processes. Most warm-core SCVs are carried by the KE and enter the southern recirculation gyre, while cold-core SCVs primarily propagate along the continental slope. Based on an offline particle tracking procedure, the SCVs are found to conserve and transport water masses over long distances, trapping a water volume of $\sim 10^{11} \text{ m}^3$.

After SCVs enter the ocean interior, the horizontal extent of the vortex core slowly shrinks and the temperature contours at the vortex edge become sparse, indicating a decrease in the kinetic energy (figures not shown). For such submesoscale motion, whether the vortex erosion and associated dynamic mechanism can be described by the mixing parameterization in the simulations is not analyzed in this study. Due to the limitations of simulation duration and region, many long-lived SCVs are still present on the last day of model output, and some others have left the nested domain early. To assess their contribution to water transport in the ocean interior, model experiments with longer durations and larger areas are needed. In addition, some previous studies mentioned that Kiddies at $26.2\text{--}26.7\sigma_\theta$ may be generated through the subduction process associated with mixed layer frontogenesis in the subarctic front region (Zhang et al. 2015; Li et al. 2017), which needs to be further examined in the future.

Acknowledgments. This research is supported by the National Natural Science Foundation of China (42225601, 42076009, 42176006, 42222601, 42106015, 42225602, 92058201), and Fundamental Research Funds for the Central Universities (202072001, 202241006). Z. C. is partly supported by the Taishan Scholar Funds (tsqn201812022).

Data availability statement. Source data for ROMS simulations are available at scientific database of South China Sea Institute of Oceanology (www.scio.csdb.cn). The mooring data can be downloaded via https://cn-kems.net/Data/JPO230072_figure6.mat. Surface geostrophic current is obtained from Copernicus Marine Environment Monitoring Service at <https://doi.org/10.48670/moi-00148>.

REFERENCES

- Armi, L., D. Hebert, N. Oakey, J. F. Price, P. L. Richardson, H. T. Rossby, and B. Ruddick, 1989: Two years in the life of a Mediterranean salt lens. *J. Phys. Oceanogr.*, **19**, 354–370, [https://doi.org/10.1175/1520-0485\(1989\)019<0354:TYITLO>2.0.CO;2](https://doi.org/10.1175/1520-0485(1989)019<0354:TYITLO>2.0.CO;2).
- Barceló-Llull, B., E. Pallàs-Sanz, P. Sangrà, A. Martínez-Marrero, S. N. Estrada-Allis, and J. Arístegui, 2017: Ageostrophic secondary circulation in a subtropical intrathermocline eddy. *J. Phys. Oceanogr.*, **47**, 1107–1123, <https://doi.org/10.1175/JPO-D-16-0235.1>.
- Bashmachnikov, I., F. Neves, T. Calheiros, and X. Carton, 2015: Properties and pathways of Mediterranean water eddies in the Atlantic. *Prog. Oceanogr.*, **137**, 149–172, <https://doi.org/10.1016/j.pocean.2015.06.001>.
- Bosse, A., and Coauthors, 2016: Scales and dynamics of submesoscale coherent vortices formed by deep convection in the northwestern Mediterranean Sea. *J. Geophys. Res. Oceans*, **121**, 7716–7742, <https://doi.org/10.1002/2016JC012144>.
- , and Coauthors, 2017: A submesoscale coherent vortex in the Ligurian Sea: From dynamical barriers to biological implications. *J. Geophys. Res. Oceans*, **122**, 6196–6217, <https://doi.org/10.1002/2016JC012634>.
- , I. Fer, J. M. Lilly, and H. Sjøiland, 2019: Dynamical controls on the longevity of a non-linear vortex: The case of the Lofoten Basin eddy. *Sci. Rep.*, **9**, 13448, <https://doi.org/10.1038/s41598-019-49599-8>.
- Bower, A. S., R. M. Hendry, D. E. Amrhein, and J. M. Lilly, 2013: Direct observations of formation and propagation of subpolar eddies into the subtropical North Atlantic. *Deep-Sea Res. II*, **85**, 15–41, <https://doi.org/10.1016/j.dsr2.2012.07.029>.
- Cao, H., and Z. Jing, 2022: Submesoscale ageostrophic motions within and below the mixed layer of the northwestern Pacific Ocean. *J. Geophys. Res. Oceans*, **127**, e2021JC017812, <https://doi.org/10.1029/2021JC017812>.
- , B. Fox-Kemper, and Z. Jing, 2021: Submesoscale eddies in the upper ocean of the Kuroshio Extension from high-resolution simulation: Energy budget. *J. Phys. Oceanogr.*, **51**, 2181–2201, <https://doi.org/10.1175/JPO-D-20-0267.1>.
- Carton, J. A., and B. S. Giese, 2008: A reanalysis of ocean climate using Simple Ocean Data Assimilation (SODA). *Mon. Wea. Rev.*, **136**, 2999–3017, <https://doi.org/10.1175/2007MWR1978.1>.
- Chelton, D. B., R. A. deSzoeke, M. G. Schlax, K. El Naggar, and N. Siwertz, 1998: Geographical variability of the first baroclinic Rossby radius of deformation. *J. Phys. Oceanogr.*, **28**, 433–460, [https://doi.org/10.1175/1520-0485\(1998\)028<0433:GVOTFB>2.0.CO;2](https://doi.org/10.1175/1520-0485(1998)028<0433:GVOTFB>2.0.CO;2).
- Collins, C. A., T. Margolina, T. A. Rago, and L. Ivanov, 2013: Looping RAFOS floats in the California Current System. *Deep-Sea Res. II*, **85**, 42–61, <https://doi.org/10.1016/j.dsr2.2012.07.027>.
- D’Asaro, E. A., 1988: Generation of submesoscale vortices: A new mechanism. *J. Geophys. Res.*, **93**, 6685–6693, <https://doi.org/10.1029/JC093iC06p06685>.
- Damen, P., A. Bosse, P. Testor, P. Marsaleix, and C. Estournel, 2017: Modeling postconvective submesoscale coherent vortices in the northwestern Mediterranean Sea. *J. Geophys. Res. Oceans*, **122**, 9937–9961, <https://doi.org/10.1002/2016JC012114>.
- Delandmeter, P., and E. van Sebille, 2019: The parcels v2.0 Lagrangian framework: New field interpolation schemes. *Geosci. Model Dev.*, **12**, 3571–3584, <https://doi.org/10.5194/gmd-12-3571-2019>.

- Dong, J., Z. Jing, B. Fox-Kemper, Y. Wang, H. Cao, and C. Dong, 2022: Effects of symmetric instability in the Kuroshio Extension region in winter. *Deep-Sea Res. II*, **202**, 105142, <https://doi.org/10.1016/j.dsr2.2022.105142>.
- Freeman, E., and Coauthors, 2017: ICOADS release 3.0: A major update to the historical marine climate record. *Int. J. Climatol.*, **37**, 2211–2232, <https://doi.org/10.1002/joc.4775>.
- Frenger, I., D. Bianchi, C. Stührenberg, A. Oschlies, J. Dunne, C. Deutsch, E. Galbraith, and F. Schütte, 2018: Biogeochemical role of subsurface coherent eddies in the ocean: Tracer cannonballs, hypoxic storms, and microbial stewpots? *Global Biogeochem. Cycles*, **32**, 226–249, <https://doi.org/10.1002/2017GB005743>.
- Garfield, N., C. A. Collins, R. G. Paquette, and E. Carter, 1999: Lagrangian exploration of the California Undercurrent, 1992–95. *J. Phys. Oceanogr.*, **29**, 560–583, [https://doi.org/10.1175/1520-0485\(1999\)029<0560:LEOTCU>2.0.CO;2](https://doi.org/10.1175/1520-0485(1999)029<0560:LEOTCU>2.0.CO;2).
- Graves, L. P., J. C. McWilliams, and M. T. Montgomery, 2006: Vortex evolution due to straining: A mechanism for dominance of strong, interior anticyclones. *Geophys. Astrophys. Fluid Dyn.*, **100**, 151–183, <https://doi.org/10.1080/03091920600792041>.
- Gula, J., M. J. Molemaker, and J. C. McWilliams, 2015: Topographic vorticity generation, submesoscale instability and vortex street formation in the Gulf Stream. *Geophys. Res. Lett.*, **42**, 4054–4062, <https://doi.org/10.1002/2015GL063731>.
- , T. M. Blacic, and R. E. Todd, 2019: Submesoscale coherent vortices in the Gulf Stream. *Geophys. Res. Lett.*, **46**, 2704–2714, <https://doi.org/10.1029/2019GL081919>.
- Haynes, P. H., and M. E. McIntyre, 1987: On the evolution of vorticity and potential vorticity in the presence of diabatic heating and frictional or other forces. *J. Atmos. Sci.*, **44**, 828–841, [https://doi.org/10.1175/1520-0469\(1987\)044<0828:OTEOVA>2.0.CO;2](https://doi.org/10.1175/1520-0469(1987)044<0828:OTEOVA>2.0.CO;2).
- Hebert, D., N. Oakey, and B. Ruddick, 1990: Evolution of a Mediterranean salt lens: Scalar properties. *J. Phys. Oceanogr.*, **20**, 1468–1483, [https://doi.org/10.1175/1520-0485\(1990\)020<1468:EOAMSL>2.0.CO;2](https://doi.org/10.1175/1520-0485(1990)020<1468:EOAMSL>2.0.CO;2).
- Hoskins, B. J., 1974: The role of potential vorticity in symmetric stability and instability. *Quart. J. Roy. Meteor. Soc.*, **100**, 480–482, <https://doi.org/10.1002/qj.49710042520>.
- Jagannathan, A., K. Srinivasan, J. C. McWilliams, M. J. Molemaker, and A. L. Stewart, 2021: Boundary-layer-mediated vorticity generation in currents over sloping bathymetry. *J. Phys. Oceanogr.*, **51**, 1757–1778, <https://doi.org/10.1175/JPO-D-20-0253.1>.
- Jing, Z., B. Fox-Kemper, H. Cao, R. Zheng, and Y. Du, 2021: Submesoscale fronts and their dynamical processes associated with symmetric instability in the northwest Pacific subtropical ocean. *J. Phys. Oceanogr.*, **51**, 83–100, <https://doi.org/10.1175/JPO-D-20-0076.1>.
- Karstensen, J., and Coauthors, 2017: Upwelling and isolation in oxygen-depleted anticyclonic mode-water eddies and implications for nitrate cycling. *Biogeosciences*, **14**, 2167–2181, <https://doi.org/10.5194/bg-14-2167-2017>.
- Kurian, J., F. Colas, X. Capet, J. C. McWilliams, and D. B. Chelton, 2011: Eddy properties in the California Current System. *J. Geophys. Res.*, **116**, C08027, <https://doi.org/10.1029/2010JC006895>.
- Large, W. G., J. C. McWilliams, and S. C. Doney, 1994: Oceanic vertical mixing: A review and a model with a nonlocal boundary layer parameterization. *Rev. Geophys.*, **32**, 363–403, <https://doi.org/10.1029/94RG01872>.
- Lemarié, F., J. Kurian, A. F. Shchepetkin, M. Jeroen Molemaker, F. Colas, and J. C. McWilliams, 2012: Are there inescapable issues prohibiting the use of terrain-following coordinates in climate models? *Ocean Modell.*, **42**, 57–79, <https://doi.org/10.1016/j.ocemod.2011.11.007>.
- Li, C., Z. Zhang, W. Zhao, and J. Tian, 2017: A statistical study on the subthermocline submesoscale eddies in the northwestern Pacific Ocean based on Argo data. *J. Geophys. Res. Oceans*, **122**, 3586–3598, <https://doi.org/10.1002/2016JC012561>.
- Lilly, J. M., and P. B. Rhines, 2002: Coherent eddies in the Labrador Sea observed from a mooring. *J. Phys. Oceanogr.*, **32**, 585–598, [https://doi.org/10.1175/1520-0485\(2002\)032<0585:CEITLS>2.0.CO;2](https://doi.org/10.1175/1520-0485(2002)032<0585:CEITLS>2.0.CO;2).
- Luo, S., Z. Jing, and Y. Qi, 2020: Submesoscale flows associated with convergent strain in an anticyclonic eddy of the Kuroshio Extension: A high-resolution numerical study. *Ocean Sci. J.*, **55**, 249–264, <https://doi.org/10.1007/s12601-020-0022-x>.
- Marshall, J., D. Jamous, and J. Nilsson, 2001: Entry, flux, and exit of potential vorticity in ocean circulation. *J. Phys. Oceanogr.*, **31**, 777–789, [https://doi.org/10.1175/1520-0485\(2001\)031<0777:EFAEOP>2.0.CO;2](https://doi.org/10.1175/1520-0485(2001)031<0777:EFAEOP>2.0.CO;2).
- Maximenko, N., and T. Yamagata, 1995: Submesoscale anomalies in the North Pacific Subarctic front. *J. Geophys. Res.*, **100**, 18459–18469, <https://doi.org/10.1029/95JC01565>.
- McCoy, D., D. Bianchi, and A. L. Stewart, 2020: Global observations of submesoscale coherent vortices in the ocean. *Prog. Oceanogr.*, **189**, 102452, <https://doi.org/10.1016/j.pcean.2020.102452>.
- McDowell, S. E., and H. T. Rossby, 1978: Mediterranean water: An intense mesoscale eddy off the Bahamas. *Science*, **202**, 1085–1087, <https://doi.org/10.1126/science.202.4372.1085>.
- McWilliams, J. C., 1985: Submesoscale, coherent vortices in the ocean. *Rev. Geophys.*, **23**, 165–182, <https://doi.org/10.1029/RG023i002p00165>.
- , 2016: Submesoscale currents in the ocean. *Proc. Roy. Soc.*, **472A**, 20160117, <https://doi.org/10.1098/rspa.2016.0117>.
- Meunier, T., and Coauthors, 2018: Intrathermocline eddies embedded within an anticyclonic vortex ring. *Geophys. Res. Lett.*, **45**, 7624–7633, <https://doi.org/10.1029/2018GL077527>.
- Molemaker, M. J., J. C. McWilliams, and W. K. Dewar, 2015: Submesoscale instability and generation of mesoscale anticyclones near a separation of the California Undercurrent. *J. Phys. Oceanogr.*, **45**, 613–629, <https://doi.org/10.1175/JPO-D-13-0225.1>.
- Okubo, A., 1970: Horizontal dispersion of floatable particles in the vicinity of velocity singularities such as convergences. *Deep-Sea Res. Oceanogr. Abstr.*, **17**, 445–454, [https://doi.org/10.1016/0011-7471\(70\)90059-8](https://doi.org/10.1016/0011-7471(70)90059-8).
- Qiu, B., K. A. Kelly, and T. M. Joyce, 1991: Mean flow and variability in the Kuroshio Extension from Geosat altimetry data. *J. Geophys. Res.*, **96**, 18491–18507, <https://doi.org/10.1029/91JC01834>.
- Sasaki, Y. N., and S. Minobe, 2015: Climatological mean features and interannual to decadal variability of ring formations in the Kuroshio Extension region. *J. Oceanogr.*, **71**, 499–509, <https://doi.org/10.1007/s10872-014-0270-4>.
- Senjyu, T., T. Ishimaru, M. Matsuyama, and Y. Koike, 1998: High salinity lens from the Strait of Hormuz. *Offshore Environment of the ROPME Sea Area after the War-Related Oil Spill – Results of the 1993–94 Umiataka-Maru Cruise*, A. Otsuki, Ed., TERRAPUB, 35–48.
- Shchepetkin, A. F., and J. C. McWilliams, 2005: The Regional Oceanic Modeling System (ROMS): A split-explicit, free-surface, topography-following-coordinate oceanic model. *Ocean*

- Modell.*, **9**, 347–404, <https://doi.org/10.1016/j.ocemod.2004.08.002>.
- Sheen, K. L., J. A. Brearley, A. C. Naveira Garabato, D. A. Smeed, L. St. Laurent, M. P. Meredith, A. M. Thurnherr, and S. N. Waterman, 2015: Modification of turbulent dissipation rates by a deep Southern Ocean eddy. *Geophys. Res. Lett.*, **42**, 3450–3457, <https://doi.org/10.1002/2015GL063216>.
- Spall, M. A., 1995: Frontogenesis, subduction, and cross-front exchange at upper ocean fronts. *J. Geophys. Res.*, **100**, 2543–2557, <https://doi.org/10.1029/94JC02860>.
- Srinivasan, K., J. C. McWilliams, M. J. Molemaker, and R. Barkan, 2019: Submesoscale vortical wakes in the lee of topography. *J. Phys. Oceanogr.*, **49**, 1949–1971, <https://doi.org/10.1175/JPO-D-18-0042.1>.
- , —, and A. Jagannathan, 2021: High vertical shear and dissipation in equatorial topographic wakes. *J. Phys. Oceanogr.*, **51**, 1985–2001, <https://doi.org/10.1175/JPO-D-20-0119.1>.
- Steinberg, J. M., N. A. Pelland, and C. C. Eriksen, 2019: Observed evolution of a California undercurrent eddy. *J. Phys. Oceanogr.*, **49**, 649–674, <https://doi.org/10.1175/JPO-D-18-0033.1>.
- Talley, L. D., 1993: Distribution and formation of North Pacific intermediate water. *J. Phys. Oceanogr.*, **23**, 517–537, [https://doi.org/10.1175/1520-0485\(1993\)023<0517:DAFONP>2.0.CO;2](https://doi.org/10.1175/1520-0485(1993)023<0517:DAFONP>2.0.CO;2).
- , 1997: North Pacific intermediate water transports in the mixed water region. *J. Phys. Oceanogr.*, **27**, 1795–1803, [https://doi.org/10.1175/1520-0485\(1997\)027<1795:NPIWTI>2.0.CO;2](https://doi.org/10.1175/1520-0485(1997)027<1795:NPIWTI>2.0.CO;2).
- Testor, P., and J.-C. Gascard, 2006: Post-convection spreading phase in the northwestern Mediterranean Sea. *Deep-Sea Res. I*, **53**, 869–893, <https://doi.org/10.1016/j.dsr.2006.02.004>.
- Thomas, L. N., 2008: Formation of intrathermocline eddies at ocean fronts by wind-driven destruction of potential vorticity. *Dyn. Atmos. Oceans*, **45**, 252–273, <https://doi.org/10.1016/j.dynatmoce.2008.02.002>.
- Thomsen, S., T. Kanzow, G. Krahnmann, R. J. Greatbatch, M. Dengler, and G. Lavik, 2016: The formation of a subsurface anticyclonic eddy in the Peru-Chile Undercurrent and its impact on the near-coastal salinity, oxygen, and nutrient distributions. *J. Geophys. Res. Oceans*, **121**, 476–501, <https://doi.org/10.1002/2015JC010878>.
- Timmermans, M.-L., J. Toole, A. Proshutinsky, R. Krishfield, and A. Plueddemann, 2008: Eddies in the Canada Basin, Arctic Ocean, observed from ice-tethered profilers. *J. Phys. Oceanogr.*, **38**, 133–145, <https://doi.org/10.1175/2007JPO3782.1>.
- Vic, C., G. Roulet, X. Capet, X. Carton, M. J. Molemaker, and J. Gula, 2015: Eddy-topography interactions and the fate of the Persian Gulf outflow. *J. Geophys. Res. Oceans*, **120**, 6700–6717, <https://doi.org/10.1002/2015JC011033>.
- Wang, Z., Q. Li, L. Sun, S. Li, Y. Yang, and S. Liu, 2015: The most typical shape of oceanic mesoscale eddies from global satellite sea level observations. *Front. Earth Sci.*, **9**, 202–208, <https://doi.org/10.1007/s11707-014-0478-z>.
- Weiss, J., 1991: The dynamics of enstrophy transfer in two-dimensional hydrodynamics. *Physica D*, **48**, 273–294, [https://doi.org/10.1016/0167-2789\(91\)90088-Q](https://doi.org/10.1016/0167-2789(91)90088-Q).
- Woodruff, S. D., and Coauthors, 2011: ICOADS release 2.5: Extensions and enhancements to the surface marine meteorological archive. *Int. J. Climatol.*, **31**, 951–967, <https://doi.org/10.1002/joc.2103>.
- Xu, A., F. Yu, and F. Nan, 2019: Study of subsurface eddy properties in northwestern Pacific Ocean based on an eddy-resolving OGCM. *Ocean Dyn.*, **69**, 463–474, <https://doi.org/10.1007/s10236-019-01255-5>.
- Yang, H., B. Qiu, P. Chang, L. Wu, S. Wang, Z. Chen, and Y. Yang, 2018: Decadal variability of eddy characteristics and energetics in the Kuroshio Extension: Unstable versus stable states. *J. Geophys. Res. Oceans*, **123**, 6653–6669, <https://doi.org/10.1029/2018JC014081>.
- Yang, Z., G. Wang, and C. Chen, 2019: Horizontal velocity structure of mesoscale eddies in the South China Sea. *Deep-Sea Res. I*, **149**, 103055, <https://doi.org/10.1016/j.dsr.2019.06.001>.
- Zhang, X., Z. Zhang, J. C. McWilliams, Z. Sun, W. Zhao, and J. Tian, 2022: Submesoscale coherent vortices observed in the northeastern South China Sea. *J. Geophys. Res. Oceans*, **127**, e2021JC018117, <https://doi.org/10.1029/2021JC018117>.
- Zhang, Z., P. Li, L. Xu, C. Li, W. Zhao, J. Tian, and T. Qu, 2015: Subthermocline eddies observed by rapid-sampling Argo floats in the subtropical northwestern Pacific Ocean in Spring 2014. *Geophys. Res. Lett.*, **42**, 6438–6445, <https://doi.org/10.1002/2015GL064601>.
- , Y. Zhang, and W. Wang, 2017: Three-compartment structure of subsurface-intensified mesoscale eddies in the ocean. *J. Geophys. Res. Oceans*, **122**, 1653–1664, <https://doi.org/10.1002/2016JC012376>.
- Zhao, M., and M.-L. Timmermans, 2015: Vertical scales and dynamics of eddies in the Arctic Ocean’s Canada Basin. *J. Geophys. Res. Oceans*, **120**, 8195–8209, <https://doi.org/10.1002/2015JC011251>.
- Zhu, R., Z. Chen, Z. Zhang, H. Yang, and L. Wu, 2021: Subthermocline eddies in the Kuroshio Extension region observed by mooring arrays. *J. Phys. Oceanogr.*, **51**, 439–455, <https://doi.org/10.1175/JPO-D-20-0047.1>.